Petroleum 5 (2019) 141–160

Contents lists available at ScienceDirect

Petroleum

journal homepage: www.keaipublishing.com/en/journals/petlm

The pseudo-homogeneous flow regime in large-scale bubble columns: experimental benchmark and computational fluid dynamics modeling

Giorgio Besagni [a, *], Fabio Inzoli [a], Thomas Ziegenhein [b], Dirk Lucas [b]

[a] Department of Energy, Politecnico di Milano, Via Lambruschini 4a, 20156, Milan, Italy
[b] Helmholtz-Zentrum Dresden-Rossendorf e. V. Institute of Fluid Dynamics, 01314 Dresden, Germany

ARTICLE INFO

Article history:
Received 18 August 2017
Accepted 12 December 2017

Keywords:
CFD
Bubble column
Large-scale
Bubble size distribution
Coalescence and break-up
Validation

ABSTRACT

A precise prediction of the fluid dynamics in bubble columns is of fundamental importance to correctly design "*industrial-scale*" reactors. It is known that the fluid dynamics in bubble columns is related to the prevailing bubble size distribution existing in the systems. In this respect, multiphase computational fluid dynamic simulations, in the Eulerian multi-fluid framework, are able to predict the local bubble size distributions and, thus, the global fluid dynamics from the fluid flow conditions and by applying modeling closured. In particular, in in "*industrial-scale*" reactors, owing to the large gas sparger openings, the "*pseudo-homogeneous*" flow regime—characterized by a wide spectrum of bubble sizes—is typically observed. Unfortunately, reliable predictions of the "pseudo-homogeneous" flow regime are limited up to now: one important drawback concerns the selection of appropriate models for the coalescence and break-up. A set of closure relations was collected at the Helmholtz-Zentrum Dresden-Rossendorf that represents the best available knowledge. Recently, the authors have extended the validation of this set of closure relations to the "*pseudo-homogeneous*" flow regime, by comparing the numerical predictions to a comprehensive experimental dataset (gas holdup, bubble size distributions and local flow measurements). Unfortunately, the previous study suffers from some limitations; in particular, in the previous experimental dataset, the bubble size distributions concerned only one axial position and a detailed characterization of the gas sparger was missing. This study contributes to the existing discussion and proposed a step ahead in the study of the "pseudo-homogenous" flow regime. To this end, we propose an experimental study, to improve the comprehensive dataset previously obtained. The novel dataset—obtained for two gas velocities—concerns bubble size distributions at different axial and radial positions and a precise characterization of the gas sparger. The comprehensive bubble size distribution dataset may serve as basis to improve the coalescence and break-up closures; conversely, the precise characterization of the gas sparger served as an improved input to the numerical simulations. The numerical results, with two different lift force implementations, have been compared with the whole dataset and have been critically analyzed. Reasons for the discrepancies between the numerical results and the experimental data have been identified and may serve as basis for future studies.

1. Introduction

Two-phase bubble columns are multiphase reactors/contacting devices where a gas phase is dispersed into a continuous phase (i.e., a liquid phase—the subject of this study—or a suspension) in the form of "*non-coalescence-induced*" bubbles or of "*coalescence-induced*" bubbles. Two-phase bubble columns are widely used in chemical, petrochemical and biochemical industries because of a number of advantages they provide in both design and operation:

* Corresponding author.
E-mail address: giorgio.besagni@polimi.it (G. Besagni).
Peer review under responsibility of Southwest Petroleum University.

Production and Hosting by Elsevier on behalf of KeAi

https://doi.org/10.1016/j.petlm.2017.12.004

Nomenclature

Acronyms

BSD	Bubble Size Distribution
CFD	Computational Fluid Dynamics
CFL	Courant Friedrichs Lewy number
GVF	Gas Volume Fraction
HZDR	Helmholtz-Zentrum Dresden-Rossendorf
iMUSIG	Inhomogeneous Multiple Size Group
RANS	Reynolds Averaged Navier Stokes
URANS	Unsteady Reynolds Averaged Navier Stokes

Non-dimensional numbers

$Eo = \frac{g(\rho_k-\rho_j)d_{eq}^2}{\sigma}$ Eötvös number
$Mo = \frac{g(\rho_k-\rho_j)\mu_k^4}{\rho_k^2\sigma^3}$ Morton number
$Re = \frac{\rho_k v_b d_{eq}}{\mu_k}$ Reynolds number

Symbols

$C_{\epsilon B}$	-, Bubble-induced turbulence coefficient in Eq. (5)
C_μ	-, Constant in Eq. (7)
C_D	-, Drag coefficient in Eq. (12)
C_L	-, Lift coefficient in Eq. (17)
C_{TD}	-, Turbulent dispersion coefficient in Eq. (24)
C_{VM}	-, Virtual mass force coefficient in Eq. (25)
C_{WL}	-, Wall force coefficient in Eq. (21)
d_{23}	mm, Sauter mean bubble diameter
d_b	mm, Bulk bubble diameter in Eq. (6)
d_{eq}	mm, Bubble equivalent diameter
$d_\perp$	mm, Maximum horizontal dimension of the bubble
d_c	mm, Diameter of the column
d_o	mm, Diameter of the column sparger openings
d_{cr}	mm, Bubble equivalent diameter for the change of sign of the lift force
f	-, Class relative frequency
$Eo_\perp$	-, Eötvös number considering the maximum horizontal dimension of the bubble $d_\perp$
F_D	kg m^{-2} s^{-2}, Drag force
F_L	kg m^{-2} s^{-2}, Lift force
F_{TD}	kg m^{-2} s^{-2}, Turbulent dispersion force
F_{VM}	kg m^{-2} s^{-2}, Virtual mass force
F_{WL}	kg m^{-2} s^{-2}, Wall force
M_I	kg m^{-2} s^{-2}, Momentum exchanges
$\vec{n}_w$	-, Unit normal to the wall pointing toward the fluid
g	m s^{-2}, Acceleration of gravity
h	m, Distance from the sparger
U_G	m s^{-1}, Gas superficial velocity
k	m^2 s^{-2}, Turbulent kinetic energy
p	Pa, Pressure
S^k	kg m^{-1} s^{-3}, Source term for the turbulent kinetic energy (bubble induced turbulence contribution) – Eq. (4)
S^ε	kg m^{-1} s^{-3}, Source term for the turbulent energy dissipation (bubble induced turbulence contribution) – Eq. (5)
S^ω	kg m^{-1} s^{-3}, Source term for the specific dissipation (bubble induced turbulence contribution) – Eq. (5)
t	s, Time
u	m s^{-1}, Velocity in governing equations
v_b	m s^{-1}, Bubble velocity
y	m, Distance to the wall

Greek letters

α	-, Volume fraction
ε_G	-, Gas holdup
$\varepsilon_{G,Local}$	-, Local void fraction
μ	kg m^{-1} s^{-1}, dynamic viscosity
ρ	kg m^{-3}, density
σ	N m^{-1}, surface tension
σ_{TD}	-, Schmidt number in Eq. (24)
$\overline{\tau}$	kg m s^{-2}, viscous and Reynolds stresses
τ	s^{-1}, Time scale

Superscripts

$\rightarrow$	Vector quantity
turb	Turbulent quantity
mol	Physical quantity
eff	effective value (turbulent and physical)

Subscripts

$\|\|$	Component of the vector parallel to the wall
cap-bubble	Cap-shape bubble
ellipse	Ellipse-shape bubble
large	large bubble gropus
small	small bubble group
sphere	Spherical-shape bubble
j	j-th dispersed phase in governing equations
k	k-th Continuous phase in governing equations
z	Generic phase in governing equations
liquid-phase	Term included in the governing equations for the liquid phase

Turbulence quantities

k	m^2 s^{-2}, Turbulent kinetic energy
ε	m^2 s^{-3}, Turbulent dissipation rate
ω	s^{-1}, Specific dissipation rate

simplicity of construction, lack of any mechanically operated parts, low energy input requirements, reasonable prices and high performance (i.e., a large contact area between the liquid and gas phase and good mixing within the liquid phase throughout the column). Despite the simple bubble column arrangement bubble columns are characterized by extremely complex interactions between the phases. When increasing the gas superficial velocity—in a large-diameter and large-scale bubble column with non-foaming liquids—the homogeneous flow regime, the transition flow regime and the heterogeneous flow regime are progressively observed (see also the flow maps of Shah et al. [1]). The homogeneous flow regime is defined as the flow regime where only "*non-coalescence-induced*" bubbles exist (e.g. as defined in Ref. [2], by the gas disengagement approach). The homogeneous flow regime can be further classified into (a) the "*mono-dispersed homogeneous*" flow regime and (b) the "*pseudo-homogeneous*" flow regime, depending

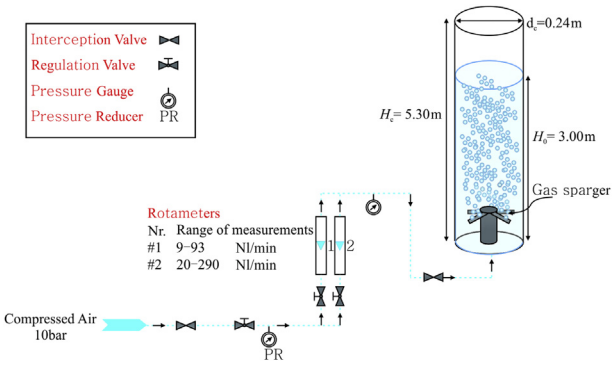

Fig. 1. The experimental setup.

on the prevailing bubble size distribution (BSD) existing in the systems (i.e., in the developed region of the two phase flow). In particular, in "*industrial-scale*" reactors, owing to the large gas sparger openings, the "*pseudo-homogeneous*" flow regime—characterized by a wide spectrum of bubble sizes—is typically observed.

Among the fluid dynamic properties, a precise estimation of the BSDs is of fundamental importance to understand the fluid dynamics and to estimate the mass transfer in bubble columns. Multiphase computational fluid dynamic (CFD) simulations, in the Eulerian multi-fluid framework, are able to predict the local BSDs from the fluid flow conditions using coalescence and breakage kernels. Unfortunately, reliable predictions of the "*pseudo-homogeneous*" flow regime are limited up to now: one important drawback concerns the selection of appropriate closure relations for (a) the momentum exchange between phases, (b) the effects of the dispersed bubbles on the turbulence of the continuous phase, and (c) the bubble coalescence and break-up phenomena. In a recent paper proposed by the authors [3], a CFD approach has been validated against a comprehensive dataset of local and global flow properties obtained in a "*pseudo-homogeneous*" flow regime (in the framework of a large-diameter and large-scale bubble column). Unfortunately, the previous study suffers from some limitations; in particular, in the previous experimental dataset, the bubble size distributions concerned only one axial position and a detailed characterization of the gas sparger was missing. The proposed paper contributes to our previous paper as follows: (a) it extends the previously obtained experimental dataset, by BSDs obtained at different axial and radial positions as well as in the gas sparger region; (b) it extends and improved the validation of the proposed approach has been further extended. In this paper, two cases with different gas superficial velocities have been investigated experimentally and numerically in the batch mode only: (i) $U_G = 0.0037$ m/s, (ii) $U_G = 0.0074$ m/s. Future studies will be devoted to extend this range as well as to study numerically also the counter-current mode.

This study contributes to the existing discussion and proposed a step ahead in the study of the "pseudo-homogenous" flow regime. The improved comprehensive BSD dataset may serve as basis to improve the coalescence and break-up closures, by the data obtained at different axial and radial positions. Furthermore, the precise characterization of the gas sparger served as an improved input to the numerical simulations. In conclusion, this comparison is a further step toward a reliable tool to simulate large-scale bubble column reactors.

2. The experimental setup and methods

The experimental facility (Fig. 1) is a large-diameter and large-scale bubble[1] column made of Plexiglas® with $d_c = 0.24$ m and $H_c = 5.3$ m. Please note that the bubble column has been built accordingly with the well-known scale-up criteria (i.e., see ref. [4]). A pressure reducer controls the pressure upstream from the rotameters (1) and (2), used to measure the gas flow rate (accuracy ± 2% f.s.v., E5-2600/h, manufactured by ASA, Italy). The spider sparger (an example of industrial-type distributors, Fig. 2a) has six arms made of 0.012 m diameter stainless steel tubes soldered to the center cylinder of the sparger. The gas sparger has been installed with the six holes ($d_o = 2–4$ mm, where d_o is the diameter of the gas sparger opening) located on the side of each arm facing upward; these holes are distributed as shown in Fig. 2b and c, with an increasing diameter moving toward the column wall. The reader should refer to our previous papers for other photos and detailed descriptions of the spider sparger design and the experimental facility as well (i.e., ref. [5]).

In our previous paper [2] we have applied a variety of experimental techniques to investigate the bubble column fluid dynamics: (a) gas holdup, (b) gas disengagement, (c) image analysis and (d) optical probe measurements. The gas holdup and gas disengagement measurements were used to investigate the flow regime transition from the homogeneous towards the transition flow regimes. The image analysis was used to study the bubble shapes and size distributions near the sparger and in the developed region of the column. The optical probe was used to acquire radial profiles of the local properties (i.e., local void fraction, $\varepsilon_{G,Local}$, and bubble rise velocity). As mentioned in the introduction, the previous experimental study suffered from some limitations. To this end, we propose an experimental study, to improve the comprehensive dataset previously obtained. In particular, bubble size distributions at different axial and radial positions were obtained along with a detailed characterization of the gas sparger.

The novel experimental investigation have been performed by using the image analysis tool previously applied in our other studies to sample (i) spherical/ellipsoidal and (ii) distorted bubbles [2,6]. The photos have been taken using a NIKON D5000 camera (general settings as follow: Nikon 10–24 mm lenses, f/3.5; 1/1600s; ISO400; 4288 × 2848 pixels and a spatial resolution of 11.8 pixel/mm). A 500 W LED halogen lamp has been used as light source. Visualization sections consist in squared boxes (filled with water)

[1] The diameter of the column, its height and the sparger openings have been chosen considering the well-known scale up criteria reported in the literature: generally, a diameter greater than $d_c > 0.15$ m, an aspect ratio (the ratio between the liquid free level and the column diameter) larger than 5 and sparger openings larger than $d_o > 1$ mm guarantee results that could be used for scaling up, accordingly with the widely accepted scale-up criteria of Wilikinson et al. (Wilkinson et al., 1992).

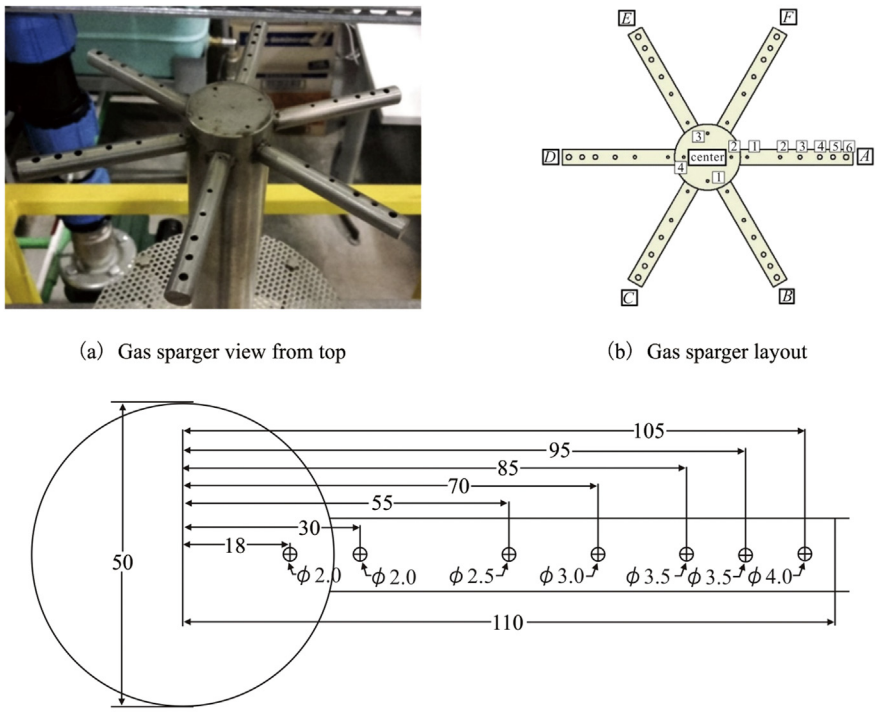

(a) Gas sparger view from top

(b) Gas sparger layout

(c) Spider sparger: distribution of the holes on one of the six arms (measurements in mm)

Fig. 2. The spider sparger.

Table 1
Location of image acquisition.

Distance from the gas spargerfrom sparger [m]	
Center region	Wall region
0	
0.25	0.35
1	1.05
1.45	1.55
2.2	2.25
–	2.75

around the vertical pipe designed for correcting the distorted image. The experimental methods, uncertainties and experimental procedure have been deeply detailed in our previous paper and, for this reason they are not repeated here (see, for example, refs. [2,6,7]. Photos have been taken at different axial location in the bubble column; in the sparger region, the camera has bene focused on the gas sparger openings; conversely, to study the BSDs evolution inside the bubble column, the camera has been focused on (a) a ruler along the external wall and (b) a rules one inside the column, to study the influence of the radial location on BSDs (see Ref. [2] for further details on this method). The location where images have been acquired are summarized in Table 1.

3. The experimental results

In this section, the experimental dataset obtained has been presented and discussed. First, the BSDs at the sparger region have been discussed (an example of bubble size in these region is proposed in Fig. 3); secondly, the axial evolution of the BSDs in the bubble column (an example of bubble size in these regions is proposed in Fig. 4) has been presented and discussed for the two superficial gas velocities studied: (i) $U_G = 0.0037$ m/s, (ii) $U_G = 0.0074$ m/s. It is worth noting that the image analysis to characterize the gas sparger has been performed by using the method proposed in Ref. [2].

3.1. Sparger region

The spider sparger is classified as a "*coarse sparger*", owing to the large sparger opening. Therefore, a "*pseuso-homogeneous*" flow regime is produced and a maldistribution flow regime takes place at low gas flow rates [2]. In these conditions, a precise characterisation of the BSDs produced by the different sparger openings is of fundamental importance to correctly model the inlet region of the bubble column.

Therefore, the aim of the image analysis near the gas sparger is twofold: (a) provide inlet conditions for the numerical approach; (b) provide data and methods that can be easily used by other researchers to model "*coarse spargers*". To this end, a precise description of the BSDs generated by the different gas sparger openings (Fig. 2c) is proposed. To this end, a main assumption was made: exists. The BSDs produced by the same sparger opening (the same number on Fig. 2b) do not depend on the sparger arm selected (radial symmetry for the BSDs). This assumption led, as a result, to seven equivalent diameter BSDs for each flow rate, one for the central holes and the other six for the holes in the arms. The obtained experimental data, to be easily implemented in the numerical approach and easily used by other researchers, were, subsequently, fitted by log-normal distributions, as suggested by Refs. [8–10]:

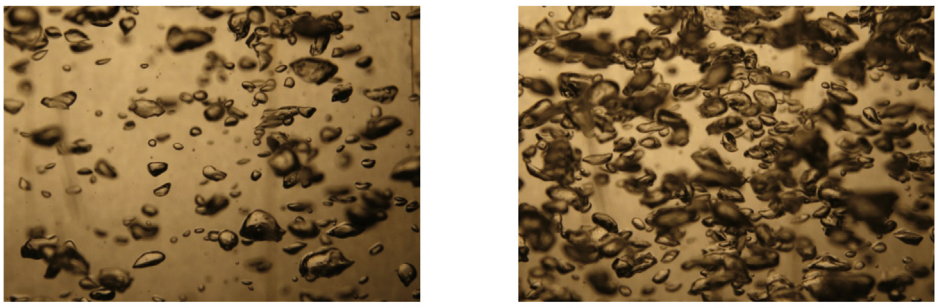

(a) U_G=0.0037 m/s (b) U_G=0.0074 m/s

Fig. 3. Gas sparger region: flow visualizations.

(a) U_G=0.0037 m/s (b) U_G=0.0074 m/s

Fig. 4. Developed region: flow visualizations.

$$\ln\mathcal{N}(x;\mu,\sigma) = \frac{1}{x\sigma\sqrt{2\pi}} exp\left[-\frac{(\ln x-\mu)^2}{2\sigma^2}\right] \quad (1)$$

Table 2 presents the results of the analysis and the parameters to be included in Eq. (1). As expected, the mean bubble diameter seems to be proportional to the one of the hole from which it was released [11]. The larger the hole, the larger the variance or, equivalently, the standard deviation found for the distribution. To the authors' best knowledge this characterisation of the BSDs at the gas sparger was proposed for the first time in the literature.

Table 2
Results of the sparger data analysis. Parameters refer to Eq. (1). Code reference for hole number refers to Fig. 2b.

Hole	d_o [mm]	U_G [m/s]	0.0037	0.0074
0		μ	10.89	12.76
	2	σ	0.2536	0.1850
		SSR	0.00696	0.00432
1		μ	6.33	8.78
	2	σ	0.2370	0.2946
		SSR	0.02592	0.05221
2		μ	9.97	11.08
	2.5	σ	0.3143	0.3346
		SSR	0.03562	0.03807
3		μ	11.74	13.89
	3	σ	0.3168	0.2127
		SSR	0.09140	0.01139
4		μ	12.05	13.33
	3.5	σ	0.2852	0.3141
		SSR	0.03694	0.04918
5		μ	9.43	10.57
	3.5	σ	0.504031	0.270803
		SSR	0.091456	0.115406
6		μ	11.70	10.26
	4	σ	0.3095	0.3564
		SSR	0.05245	0.03940

3.2. Axial development of BSDs

The image analysis has been applied to study the axial development of the BSDs in the bubble column: these data are of fundamental importance to validate coalescence and break-up kernels. The results of the analysis are presented in Fig. 5 ($U_G = 0.0037$ m/s) and in Fig. 6 ($U_G = 0.0074$ m/s): the system is poly-dispersed in nature and the present homogeneous flow regime is classified as "*pseudo-homogeneous*" flow regime.

The BSDs imposed by the gas sparger openings evolves in the axial direction of the bubble column, owing to the non-equilibrium between coalescence and breakup, till the equilibrium BSD is established. It is worth noting that, regardless of the axial location, all BSDs have approximately the same behavior: at the lowest gas superficial velocity BSDs are shifted towards small diameters on average. The mean diameter of the distribution is approximately 2 mm for the developing region up to 4 mm in the developed region. In addition, the BSD is more spread out in the lower region of the bubble column: indeed, in the sparger region the two-phase has not reached full development yet: coalescence and breakup phenomena are dominant in that situation and a widely-spread distribution is expected. As bubbles rise the column, coalescence

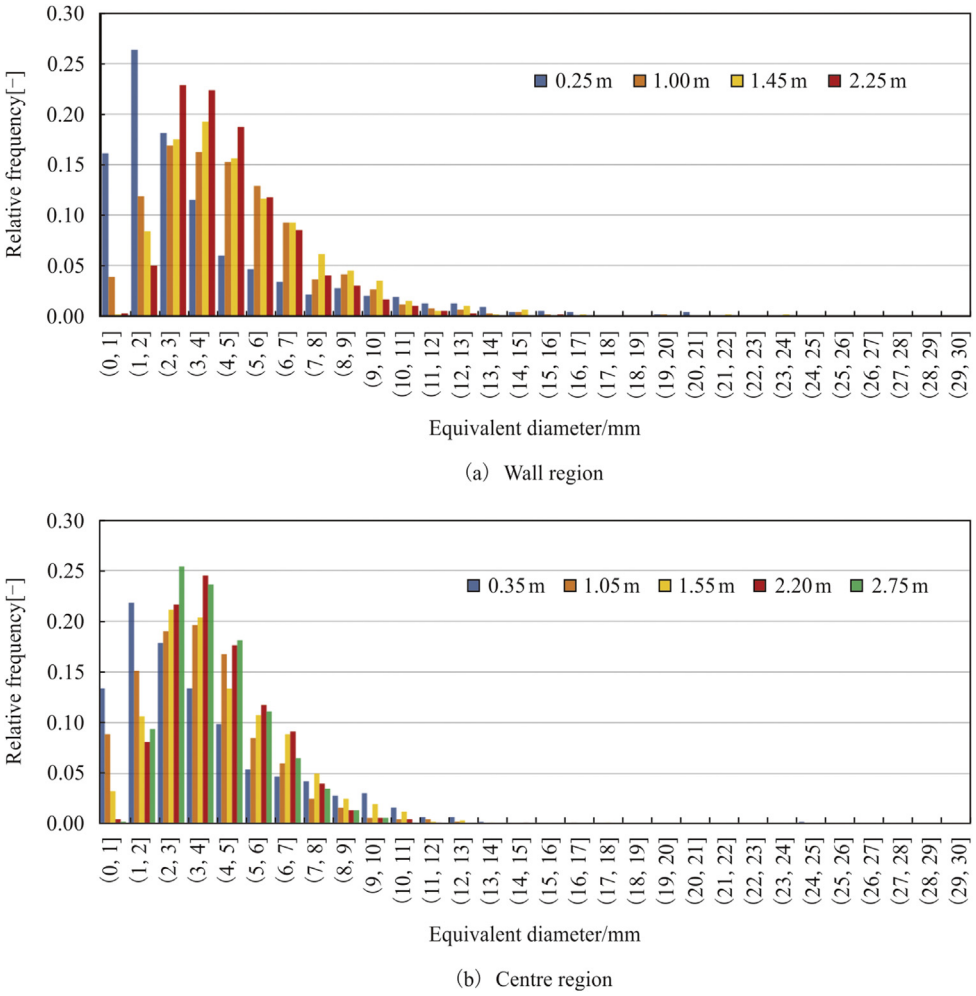

Fig. 5. Axial development of BSDs – $U_G = 0.0037$ m/s.

phenomena changes the BSDs and it shifts towards higher equivalent diameters, up to about 4–5 mm. Subsequently, the BSDs stabilize their mean diameter value and the BSDs tend to become progressively more and more centred on the mean value. This is a consequence of reaching the developed BSD. Indeed, coalescence and breakup reach an equilibrium characterized by a certain mean bubble diameter and bubbles much bigger and much smaller than that will tend, in steady state conditions, to break or coalesce, respectively, reaching a dynamic equilibrium. This observation support the discussion proposed in our very recent paper concerning the influence of the aspect ratio on bubble column fluid dynamics [12]. It is worth noting that as gas flow rate is increased, the distribution slightly shifts towards larger equivalent diameters (possibly because of coalescence phenomena).

Comparing BSDs near the wall and at the center of the bubble column, at the different axial coordinates, it is observed that BSDs near the wall are on average slightly smaller than the ones in the center section (the mean diameter at wall and center are about 3 and 4 mm, respectively), possibly because of the effect of the lift force, as discussed in our previous papers [2]. Indeed, the large bubbles, having a negative lift coefficient, tend to migrate from the low liquid velocity region towards the high liquid velocity regions (Lucas et al., 2005; Tomiyama et al., 2002): in the batch mode, the larger bubbles tend to migrate toward the center of the column. It is worth noting the different shape of the near-wall and center bubble size distributions: the ones related to the wall of the columns have a very small variance if compared to the ones at the center, namely the center bubble size distributions are much more spread out on the whole diameters range with respect to the wall. This result supports the fact that the bubbles in the center section are larger than the ones at wall. This result is observed at every vertical coordinate analyzed in this work. The only exceptions are the first axial positions (approximately 0.3 m above the distributor itself), where the bubble distribution at the center has smaller mean diameter than the one at wall. One possible explanation for that is that the flow rate exiting the sparger is highest in the column center region.

4. The physical modeling

4.1. The governing equations in the Eulerian Framework

An Eulerian two-fluid approach is adopted in the present numerical simulations. Within such a framework, the Navier-Stokes

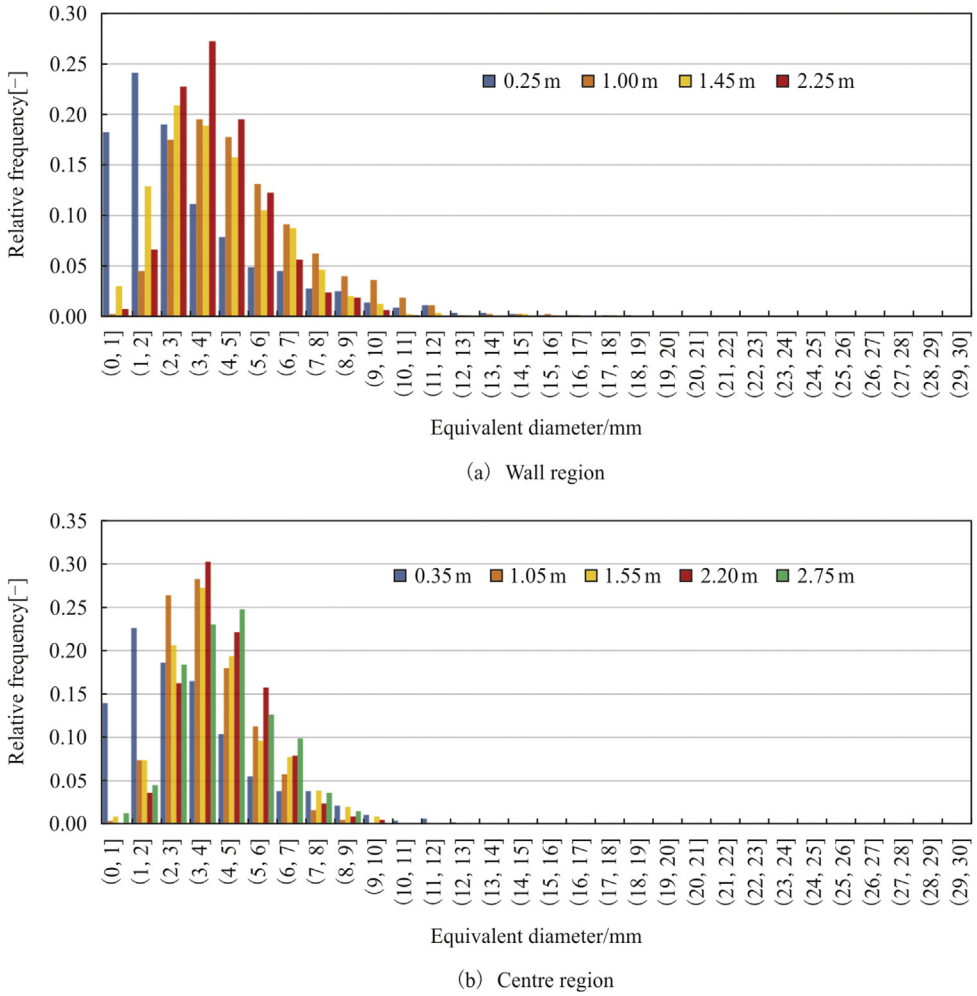

Fig. 6. Axial development of BSDs – $U_G = 0.0074$ m/s.

equations for each phase are ensemble-averaged, and the effects of turbulence and interphase phenomena have to be taken into account using closure models [13]. The reader may also refer to the dissertation of Ziegenhein for a complete discussion concerning the Eulerian Framework [14].

For an isothermal flow without mass transfer, the URANS governing equations for the generic z-th phase are:

$$\frac{\partial}{\partial t}(\alpha_z \rho_z) + \nabla \cdot (\alpha_z \rho_z \overrightarrow{u}_z) = 0 \tag{2}$$

$$\frac{\partial}{\partial t}(\alpha_k \rho_k \overrightarrow{u}_k) + \nabla \cdot (\alpha_z \rho_z \overrightarrow{u}_z \overrightarrow{u}_z) = -\alpha_z \nabla p + \nabla \cdot (\alpha_z \overline{\tau}_z) + \alpha_Z \rho_z \overrightarrow{g} + \overrightarrow{M}_{I,z} \tag{3}$$

In the following, the dispersed phase is listed as j and the continuous phase as k.

The terms on the right-hand side of Eq. (3) represent the pressure gradient, the stresses (viscous and Reynolds), the body forces and the interfacial momentum exchanges between the phases including the closure models, respectively.

The closure models for the momentum exchange are formulated as forces acting on the liquid and dispersed phases: developing and validation of such is an active filed of research and, in the present work, a model set that has been applied recently with promising success over a large experimental is used, which is from now on named as baseline model (please refer to the discussion in the Introduction and to refs. [15–23]).

In general a transient formulation is necessary to cover all flow situations, stationary flow situations are then included as special case. This is taken into account by using the unsteady Reynolds averaged Navier Stokes equations (URANS) with the two-equation$k$-ω SST turbulence model. A class method is used to model a wide BSD as well as coalescence and break-up, monodispersed bubbly flows are included as a special case with one bubble size class (please, refer to Section 3.2). Each part of the model is described in the following subsections. For further details, the reader should refer to the above-mentioned references.

4.2. The turbulence modeling

The two-equation$k$-ω SST model is used for the continuous phase. On the contrary, due to the small density, the turbulence in the dispersed gas is neglected (see Ref. [20]). Bubble induced turbulence is taken into account by adding source terms to the k-ω SST equations. The reader should refer to the studies of Rzehak and Krepper [20,24] for the investigations concerning the most suitable

choices for the additional source terms in the equations. A plausible approximations is that all energy lost by the bubble due to the drag is converted to turbulent kinetic energy of the liquid phase:

$$S^{k}_{liquid-phase} = \overrightarrow{F}_{D,j} \cdot (\overrightarrow{u}_j - \overrightarrow{u}_k) \tag{4}$$

where $\overrightarrow{F}_D$ indicates the drag force and the sub-script k-phase indicates That Eq. (4) is included as a source term in the governing equations for the turbulent kinetic energy of the liquid phase.

For the ε-source a similar heuristic is used as for the single phase model, namely the k-source is divided by a time scale τ: It follows:

$$S^{\varepsilon}_{k-phase} = C_{\varepsilon B}\frac{S^{k}_{k-phase}}{\tau} \tag{5}$$

$C_{\varepsilon B} = 1.0$ has been found to give reasonable results for air/water turbulent bubbly flows. The modeling of the time scale τ proceeds largely based on dimensional analysis. In particular, there are two velocity and two length scales for this problem, where one of each is related to the bubble and the other to the turbulent eddies, so four plausible time scales can be formed. All the different four time scales have been compared by Rzehak and Krepper [20] and it has been found that the best predictions have been obtained for:

$$\tau = \frac{d_b}{\sqrt{k_k}} \tag{6}$$

where d_b indicates the bubble bulk diameter, as indicated in Ref. [20]. Please remember that the subscript k indicates the continuous phase.

Finally, the ε-source is transformed to an equivalent ω-source which gives:

$$S^{\omega}_{k-phase} = \frac{1}{C_{\mu}k_k}S^{\varepsilon}_{k-phase} - \frac{\omega_k}{k_k}S^{k}_{k} \tag{7}$$

The ω-source in Eq. (7) is used independently of the blending function in the SST model since it should be effective throughout the domain. Since bubble-induced effects are included in k and ε/ω due to the respective source terms, the turbulent viscosity is evaluated from:

$$\mu^{turb}_{k} = C_{\mu}\rho_k\frac{k^2_k}{\varepsilon_k} \tag{8}$$

where the model constant is $C_{\mu} = 0.09$ like in single-phase flows.

Finally, the effective viscosity is computed as:

$$\mu^{eff}_{k} = \mu^{mol}_{k} + \mu^{turb}_{k} \tag{9}$$

4.3. The bubble forces

The interactions between the continuous and the disperse phases are taken into account by means of source terms in the momentum equation. In particular, considering the continuous phase k, the last term in Eq. (3) comprises several independent physical mechanisms: drag, lift, virtual mass, turbulent dispersion and wall lubrication forces:

$$\overrightarrow{M}_{I,k} = \overrightarrow{F}_{D,k} + \overrightarrow{F}_{L,k} + \overrightarrow{F}_{VM,k} + \overrightarrow{F}_{TD,k} + \overrightarrow{F}_{WL,k} \tag{10}$$

Modeling and validation of forces acting on a bubble have been intensively studied over the last decade. All forces act together to produce observable phenomena, such as, for example, the distribution of the void fraction [25]. Therefore, a complete set of interfacial forces should be used, as stated in the introduction. A complete discussion of this approach can be found in the paper of Rzehak and Krepper [20]. The drag, lift, turbulent dispersion and wall lubrication forces are implemented in the numerical model for every bubble class implemented (please, refer to Section 3.2 for further details).

The source term (in the momentum equation) for the continuous phase is, then, equal to the negation of the sum of the dispersed phase source terms:

$$\overrightarrow{F}_k = -\sum_{j=1}^{2}\overrightarrow{F}_j \tag{11}$$

4.3.1. The drag force

The drag force originates from the presence of a slip velocity between the gas and liquid phases. The corresponding gas-phase momentum source is given by:

$$\overrightarrow{F}_{D,j} = -\frac{3}{4}\alpha_j\rho_k\frac{C_D}{d_j}|\overrightarrow{u}_j - \overrightarrow{u}_k|(\overrightarrow{u}_j - \overrightarrow{u}_k) \tag{12}$$

where, C_D is the drag coefficient, ρ_k is the liquid density, α_J is the local gas fraction (local void fraction), d_j represents the diameter of the disperse phase, and $\overrightarrow{u}_j - \overrightarrow{u}_k$ is the relative velocity between the gas and the liquid phases. Within the approach used, the drag coefficient (included in the formulation of the drag force) between the continuous phase and the dispersed phases, C_D, is computed using the correlation of Ishii and Zuber [26], that distinguishing different shape flow regimes:

$$C_D = \max\left(C_{D,sphere}, \min\left(C_{D,ellipse}, C_{D,cap-bubble}\right)\right) \tag{13}$$

where:

$$C_{D,sphere} = \frac{24}{\mathrm{Re}}\left(1 + 0.1\mathrm{Re}^{0.75}\right) \tag{14}$$

$$C_{D,ellipse} = \frac{2}{3}\sqrt{\mathrm{Eo}} \tag{15}$$

$$C_{D,cap-bubble} = \frac{8}{3} \tag{16}$$

where Re and *Eo* are the Reynolds and Eötvös number respectively (please, refer to the nomenclature for the definition of these non-dimensional groups).

This correlation has been compared with an extensive data set on the terminal velocity of bubbles rising in quiescent liquids covering several orders of magnitude for each of *Re, Eo* and *Mo* (the Morton number) with good agreement except at high values of *Eo*. Ongoing studies are devoted to the calibration of drag forces to the case of dense bubbly flows and the heterogeneous regime.

No drag force interaction is taken into account between the dispersed phase classes.

4.3.2. The lift force

A bubble moving in an unbounded shear flow experiences a force perpendicular to the direction of its motion. The momentum source corresponding to this shear lift force, often simply referred to as lift force, can be calculated as:

$$\vec{F}_{L,j} = -C_L \alpha_j \rho_k (\vec{u}_j - \vec{u}_k) \times (\nabla \times \vec{u}_k) \tag{17}$$

where, C_L is the lift coefficient, ρ_k is the liquid density, α_j is the local gas fraction and $\vec{u}_j - \vec{u}_k$ is the relative velocity between the gas and the liquid phases.

4.3.2.1. Tomiyama et al. (2002) lift force. The sign of the lift coefficient is positive for "*small bubbles*" and it is negative for "*large bubbles*". The change of sign of the lift coefficient defines a critical bubble diameter, d_{cr}: for this reason, the direction of the lift force depends upon the bubble size and shape. For "*small bubbles*", the lift force acts in the direction of decreasing liquid velocity (i.e., in case of batch or co-current mode in the direction toward the pipe wall), while for "*large bubbles*" it changes direction (a force that can be assimilated to the lift force tends to push large and deformed bubbles towards the center of the column [27,28]). This is also confirmed by the DNS studies of Lu et al. [29], Lu and Tryggvason [30,31] and Santarelli and Fröhlich [32]. To account for this dependency, the model of Tomiyama et al. [28] is used to compute the lift coefficient together with the use of two bubble classes as introduced previously. One of the bubble classes represents small and nearly spherical bubbles with a positive C_L, while the other one models large and deformed bubbles with a negative C_L. For the air-water system at ambient conditions, the bubble diameter at which the change in sign occurs is $d_{cr} = 5.8$ mm. The model of Tomiyama et al. [28] is used to compute the lift coefficient:

$$C_L = \begin{cases} \min[0.288 \tanh(0.121\mathrm{Re}), f(Eo_\perp)] & Eo_\perp \leq 4 \\ f(Eo_\perp) & 4 < Eo_\perp \leq 10 \\ -0.27 & 10 < Eo_\perp \end{cases} \tag{18}$$

where:

$$f(Eo_\perp) = 0.00105 Eo_\perp^3 - 0.0159 Eo_\perp^2 - 0.0204 Eo_\perp + 0.474 \tag{19}$$

where d_{eq} is the equivalent diameter of the bubble and $Eo_\perp$ is the Eötvös number considering the maximum horizontal dimension of the bubble $d_\perp$, given by the empirical correlation for the aspect ratio by Wellek et al. [33]:

$$d_\perp = d_{eq}\left(1 + 0.163 Eo^{0.757}\right)^{1/3} \tag{20}$$

It is worth noting that the correlation of Wellek et al. [33] has been obtained for droplets in liquids and ongoing studies are devoted to clearly identify whether it can be applied to other systems or not (See, for example, refs. [34]).

This formulation of the lift coefficient is particularly interesting because it is able to distinguish between the two bubble classes as introduced previously. One of the bubble classes represents small and nearly spherical bubbles with a positive C_L, while the other one models large and deformed bubbles with a negative C_L. For the air-water system at ambient conditions, the bubble diameter at which the change in sign occurs is $d_{cr} = 5.8$ mm. The experimental conditions on which Eq. (16) is based, have been limited to the range $-5.5 \leq log_{10}Mo \leq -2.8$, $1.39 \leq Eo \leq 5.74$ and values of the Reynolds number based on bubble diameter and shear rate $0 \leq Re \leq 10$. The water-air system at normal conditions has a Morton number $log_{10}Mo = -10.58$ which is quite different, but good results have nevertheless been reported for this case [35].

4.3.2.2. Modified lift force (NewLift). As observed in our previous study [3], despite the Tomiyama lift force model has been widely implemented in simulations, experimental data from this work show a discrepancy with its predictions. In particular, the value of the bubble diameter at which the lift sign change occurs, appears to be overestimated at a value of 5.80 mm, whereas experiments seem to suggest a lower value, closer to 5 mm. Indeed, the bubbles for air-water systems (both single bubbles and dense bubbly flows) are more oblate at smaller sizes than the Wellek et al. [33] correlation predicts, which lead to a negative lift force coefficient at smaller spherical equivalent bubble sizes so that a center peak in the experiments is observed and in the simulation not. For this reason, the Wellek at al. correlation has been replaced with our correlation [34], to predict the change of the sign of the lift force at approximately 5.44 mm. The Tomiyama et al. lift force and the NewLift force have been compared in the discussion of the results.

4.3.3. The wall force

A bubble moving near a wall is subject to a lift force that pushes it away from the wall. This force is often mentioned as the wall lubrication force and is implemented as:

$$\vec{F}_{WL,j} = -C_{WL} \rho_k \alpha_j \left| (\vec{u}_k - \vec{u}_j)_{||} \right|^2 \vec{n}_w \tag{21}$$

where C_{WL} is the wall lubrication coefficient, ρ_k is the liquid density, α_j is the local gas fraction, $(\vec{u}_k - \vec{u}_j)_{||}$ is the relative velocity component parallel to the wall and $\vec{n}_w$ is the unit normal to the wall pointing toward the fluid.

C_{WL} depends mainly on the distance to the wall and is expected to be positive so the bubble is driven away from the wall. The wall lubrication coefficient (included in the formulation of the wall force, Eq. (21)), C_{WL}, is given here by the Hosokawa et al. [36] model:

$$C_{WL}(y) = f(Eo)\left(\frac{d_{eq}}{2y}\right)^2 \tag{22}$$

where y is the distance to the wall and *f(Eo)*, in the limit of small Morton number, can be computed as follows [36]:

$$f(Eo) = 0.0217 Eo \tag{23}$$

This model is based on the functional dependence obtained by Hosokawa et al. [36] starting from the observation of Tomiyama et al. [37] of single bubble trajectories in simple shear flow of a glycerol water solution. The experimental conditions on which Eq. (23) is based are $2.2 \leq Eo \leq 22$ and $log_{10}Mo = -2.5 \ldots -6.0$, but Rzehak et al. [18] has shown that good predictions are obtained also for air bubbles in water.

4.3.4. The turbulent dispersion force

Burns et al. [38] have derived a formulation for the turbulent dispersion force by Favre averaging the inter-phase drag term. It is implemented and reads as:

$$\vec{F}_{TD,j} = -\frac{3}{4} C_{TD} \alpha_j (1 - \alpha_j) \frac{C_D}{d_j} |\vec{u}_j - \vec{u}_k| \frac{\mu_k^{turb}}{\sigma_{TD}} \left(\frac{\nabla \alpha_j}{\alpha_j} - \frac{\nabla \alpha_k}{\alpha_k}\right) \tag{24}$$

where C_{TD} is the turbulent diffusion coefficient and σ_{TD} is referred to a Schmidt number (in analogy to molecular diffusion). In this approach, $C_{TD} = 1$ and $\sigma_{TD} = 0.9$. In principle it should be possible to

obtain σ_{TD} value from single bubble experiments also for this force by evaluating the statistics of bubble trajectories in well-characterized turbulent flows but to our knowledge, this has not been done yet.

4.3.5. The virtual mass

When a bubble is accelerated, a certain amount of liquid has to be set into motion as well. This may be expressed as a force acting on the bubble as:

$$\overrightarrow{F}_{VM} = C_{VM}\alpha_G\rho_L\left(\frac{D\overrightarrow{u_j}}{Dt} - \frac{D\overrightarrow{u_k}}{Dt}\right) \quad (25)$$

where $D\overrightarrow{u_j}/Dt$ and $D\overrightarrow{u_k}/Dt$ denote material derivatives with respect to the velocity of the indicated phase and C_{VM} is the virtual mass coefficient.

The virtual mass force is implemented with a $C_{VM} = 0.5$ as suggested by Mougin and Magnaudet [39].

4.4. The discrete phase modeling approaches

As discussed in our previous paper [3], when modeling the discrete phase, one should distinguish three approaches depending on the prevailing bubble sizes in the systems and the local phenomena: (a) fixed mono-dispersed approach; (b) fixed poly-dispersed approach; (c) poly-dispersed approach with bubble coalescence and break-up. As demonstrated in our previous paper, coalescence and break-up cannot be neglected in the system considered; therefore the baseline model can be applied with the "*inhomogeneous population balance model*". In particular, the inhomogeneous multiple size group (iMUSIG) model as introduced by Krepper et al. [40] has been used. This approach splits the BSD into bubble size classes and, then, assigns the bubble size classes to different velocity groups. Each velocity group, therefore, has its own velocity field. This is important to describe effects like the bubble size-dependent movement of the gas phase caused by the lift force. In particular, two velocity groups can be assigned depending on the equivalent diameter for the change in sign of the lift force. The changes in the bubble size distributions are given by coalescence and break-up kernels. Depending on these kernels, the changes in bubble size distributions are modeled by changes in the bubble frequencies in the different bubble groups. The bubble coalescence and break-up modelling is a weak point in all the simulations published on bubbly flows. For this reason, Liao and Lucas reviewed all the available models [41,42]. Then, a model combining the different mechanisms leading to bubble coalescence and break-up has been established and applied in the frame of the baseline model by Liao et al. (2015). In conclusion, this approach couples the coalescence and break-up mechanisms proposed by Liao et al. (2015) in the Inhomogeneous Multiple Size Group (iMUSIG) model proposed by Krepper et al. (2008).

In the present work, 2 velocity fields are solved and 16 bubble size classes/groups represent the dispersed phase. The velocity fields are selected accordingly with the change of sign of the lift force: a "*small*" bubble velocity field (for bubbles having $d < d_{cr}$) and a "*large*" bubble velocity field (for bubbles having $d > d_{cr}$). The inputs for the simulations have been obtained by the image analysis and he BSD provided at the input is modelled as histogram of 22 classes (from $d_{eq} = 0$ mm−22 mm). Each class represent a size group in the iMUSIG model:

(1) The "*small*" bubble velocity group is constituted of 3 bubble size groups ($d_{eq} < d_{cr}$);

(2) The "*large*" bubble velocity group is constituted of 8 bubble size groups ($d_{eq} > d_{cr}$);

4.5. The numerical settings, the simulation procedure and the boundary conditions

4.5.1. The numerical settings and simulation procedure

Three-dimensional and transient simulations have been carried out. Indeed, three-dimensional simulations are required for accurate predictions of the gas-liquid flows in bubble columns [43–46]. The numerical simulations have been performed on a mesh of 150000 elements, where the sparger has been modeled considering a simplified three-dimensional structure: (i) the lateral arms are simplifies as two-dimensional plains and (ii) the central structure has been modelled as a cylinder. Tetra cells near the sparger and hexahedral cells in the other region of the column compose the mesh. It is worth noting that the correct modeling of the three-dimensional sparger structure is required in order to capture the structures below the sparger that may influence the bubble column fluid dynamics. For transient simulations, it must be guaranteed that the solution is independent of the time step and of the mesh size. A grid resolution study was conducted to ensure that convergence with respect to the spatial resolution has been achieved. The grid resolution study is presented and discussed in our previous paper. The time discretization is characterized by using the Courant Friedrichs Lewy (*CFL*) number. In this respect, Ziegenhein et al. [15] remarked that, because the velocity is a function of position and time so is the *CFL* number. To get a characteristic value, the root mean square of all CFL numbers in the computational domain (*RSM(CFL)*) is calculated. They concluded that $RSM(CFL) < 1$ is enough for the time and space discretization. Taking into account this suggestion, in this study we have used a stricter approach: (i) $RMS(CFL) < 0.50$ and (ii) $CFL < 1$. Therefore, the time step is not fixed during the simulation but is increased as the flow field developed, within the two above-mentioned boundaries. The iterations within each time step are stopped when the residuals fall below 10^{-4}. The numerical results compared with experimental data are obtained as transient average over 250 s of simulation. Finally, the various numerical schemes are chosen in order to reduce the discretization error as much as possible within the ANSYS CFX CFD code.

4.5.2. The boundary conditions

Two cases are investigated: (i) $U_G = 0.0037$ m/s and (ii) $U_G = 0.0074$ m/s. Degassing boundary condition is assigned at the outlet. At the walls, a no-slip boundary condition is applied for the continuous phase and a free slip condition for the disperse phase. The volume fraction of the bubble classes at the inlet is set according with the considerations given in Section 4.4. Mass flow inlet boundary conditions have been assigned at the air distributor using source points located in the same position as the distributor holes (Fig. 2b). For each operating condition analyzed, the source point activation has been selected consistently to what was observed in the experimental setup on the basis of the visual observation. Indeed, the source points have been activated (and the corresponding mass flow rate has been selected) based on visual observation, in order to take into account the maldistribution at the gas sparger. Table 3 and Table 4 present, for the two tested cases, the size groups at the different source points, used as inlet conditions (accordingly with the log-normal BSD modeling proposed in Eq. (1) and Table 1, Section 3.1). Depending on the operating conditions, the source points are selected based on visual observation, in order to take into account the maldistribution at the gas sparger. In particular, activation coefficients as a function of the flow rate have been applied (Table 5), to

account for the gas maldistribution at the sparger. Please refer to our previous paper for the description of the gas maldistribution.

4.6. Post-processing

The numerical and the experimental bubble size distributions (in terms of relative frequency distributions and size fraction distributions, see Ref. [3]) have been compared. In particular, the size fraction distributions accordingly with Waghmare et al. [47] and Liao et al. [22]. Given a number N of classes, the GVF reads as follow:

$$GVF_i = \frac{f_i d_{eq,i}^3}{\sum_{i=1}^{N} f_i d_{eq,i}^3} \tag{26}$$

where f is the class relative frequency and $d_{eq,i}$ is the class equivalent mean diameter.

The experimental data have been obtained by image analysis (i.e., sampling bubbles from images). Therefore, the experimental results represent a zonal average, rather than single point variables, as the ones available from the computer-based simulations. In this respect, in order to compare the experimental and the numerical results, the mesh node-based data from the simulations have to be carefully averaged over the all nodes belonging to specific mesh zones. These zones have to be representative of the location from which the real bubbles were sampled, i.e. at the wall and the center section of the column at different heights. Regarding the wall section, the zone of the mesh where the results have been averaged in a volume with a circular crown shaped base, included an angle of 90° and a height of 0.2 m. The thickness of the base has been selected at a value of 0.022 m which is half of the focal depth of the camera used for the image analysis. The selection of this value is related back to the sampling technique, according to which the sampled bubbles have been chosen by their degree of sharpness. Concerning the central section, instead, the averaging zone is a parallelepiped with a height of 0.2 m, a base of 0.17 m and a depth equal to 0.044 m, which is, this time, the whole depth of field of the camera. A visual representation of such averaging zones has been shown in Fig. 7.

5. The numerical results

In this section, the experimental data have been compared to the numerical results in terms of the global (i.e., gas holdup) and local (i.e., BSD and local flow properties). The experimental dataset used for model validation consist in the experimental data described in Section 3 as well as the experimental data presented by Besagni and Inzoli [2]. The cases simulated are summarized as follows:

- $U_G = 0.0037$ m/s – Tomiyama et al. (2002) lift force;
- $U_G = 0.0037$ m/s – NewLift;
- $U_G = 0.0074$ m/s – Tomiyama et al. (2002) lift force;
- $U_G = 0.0074$ m/s – NewLift.

5.1. Gas holdup

Fig. 8 displays the relationship between the gas holdup and the simulation time. The mean value of the gas holdup is computed as the average gas holdup in time—excluding the initial transient—of the gas fraction in the whole domain. The results are summarized in Table 6. The numerical results agree with the experimental data, as the maximum relative error is approximately 10%. In addition, the capability prediction of the proposed approach improved compared with the numerical results presented in our previous paper [3]. The differences (over- and under-estimation of the gas holdup) can be understood by looking at the predicted BSDs, Section 5.2: a shift of the BSD towards smaller/larger bubbles, leads to higher/lower gas holdup value for the two flow rates, respectively. Finally, is worth noting that the modified lift force does not provide a considerable improvement compared with the well-known Tomiyama et al. (2002) formulation.

5.2. Bubble size distributions

Figs. 9–12 compare the simulation results, for both with the Tomiyama et al. (2002) and modified lift model, with the experimental data, in terms of BSDs and size fractions. Considering the state-of-the-art in two-phase population balance modelling, the present numerical results are promising and the discussion proposed in our previous numerical paper are confirmed. It is observed that the modified lift force does not seem to have a considerable influence over the numerical results (in agreement with the discussion in Section 5.1). Looking closer to the comparison between

Table 3
Velocity and Size Groups for the $U_G = 0.0037$ m/s simulation (hole number code as in Fig. 2b).

Velocity Group	Size Group diameter [mm]	Hole 0	Hole 1	Hole 2	Hole 3	Hole 4	Hole 5	Hole 6
Small bubbles $\alpha = 0.02$	1	0.0000	0.0000	0.0000	0.0000	0.0000	0.0000	0.0000
	2	0.0000	0.0000	0.0000	0.0000	0.0000	0.0026	0.0000
	3	0.0002	0.0056	0.0035	0.0018	0.0006	0.0442	0.0015
	4	0.0364	0.1477	0.1023	0.0774	0.0485	0.2385	0.0718
	5	0.9634	0.8467	0.8942	0.9207	0.9509	0.7147	0.9267
Large bubble $\alpha = 0.98$	6	0.0022	0.1941	0.0084	0.0022	0.0011	0.0121	0.0021
	7	0.0100	0.2514	0.0223	0.0073	0.0049	0.0207	0.0072
	8	0.0281	0.2241	0.0428	0.0172	0.0137	0.0306	0.0175
	9	0.0559	0.1555	0.0657	0.0319	0.0288	0.0407	0.0329
	10	0.1294	0.1127	0.1244	0.0745	0.0742	0.0728	0.0772
	12	0.2452	0.0504	0.2081	0.1603	0.1712	0.1299	0.1661
	14	0.2243	0.0098	0.1901	0.1891	0.2050	0.1460	0.1935
	16	0.1537	0.0017	0.1444	0.1800	0.1892	0.1498	0.1806
	18	0.0873	0.0003	0.0973	0.1486	0.1468	0.1444	0.1454
	20	0.0437	0.0000	0.0607	0.1112	0.1011	0.1334	0.1058
	22	0.0201	0.0000	0.0359	0.0777	0.0640	0.1196	0.0718

Table 4
Velocity and Size Groups for the $U_G = 0.0074$ m/s simulation (hole number code as in Fig. 2b).

Velocity Group	Size Group diameter [mm]	Hole 0	Hole 1	Hole 2	Hole 3	Hole 4	Hole 5	Hole 6
Small bubbles $\alpha = 0.01$	1	0.0000	0.0000	0.0000	0.0000	0.0000	0.0000	0.0000
	2	0.0000	0.0000	0.0000	0.0000	0.0000	0.0000	0.0000
	3	0.0000	0.0005	0.0000	0.0000	0.0000	0.0003	0.0000
	4	0.0000	0.0134	0.0002	0.0000	0.0000	0.0019	0.0000
	5	0.0002	0.0768	0.0020	0.0004	0.0001	0.0056	0.0004
Large bubble $\alpha = 0.99$	6	0.0022	0.1756	0.0084	0.0022	0.0011	0.0120	0.0021
	7	0.0100	0.2286	0.0222	0.0073	0.0049	0.0205	0.0072
	8	0.0281	0.2038	0.0427	0.0172	0.0137	0.0303	0.0175
	9	0.0559	0.1414	0.0655	0.0319	0.0288	0.0403	0.0328
	10	0.1294	0.1024	0.1242	0.0744	0.0742	0.0722	0.0772
	12	0.2451	0.0458	0.2077	0.1603	0.1712	0.1288	0.1660
	14	0.2242	0.0089	0.1897	0.1890	0.2050	0.1449	0.1934
	16	0.1537	0.0015	0.1441	0.1800	0.1892	0.1486	0.1805
	18	0.0873	0.0002	0.0971	0.1485	0.1467	0.1433	0.1453
	20	0.0437	0.0000	0.0605	0.1111	0.1010	0.1324	0.1058
	22	0.0201	0.0000	0.0358	0.0776	0.0640	0.1187	0.0717

Table 5
Holes activation table (code reference to Fig. 2b).

Arm letter and hole number		d_o [mm]	A [mm^2]	Area [%]	U_G [m/s]	
					0.0037	0.0074
A	1	2	3.142	1.068	0	0
A	2	2.5	4.909	1.669	0	0
A	3	3	7.069	2.403	0	0
A	4	3.5	9.621	3.271	0	0
A	5	3.5	9.621	3.271	0	0
A	6	4	12.566	4.272	0	0
B	1	2	3.142	1.068	0	0.0072
B	2	2.5	4.909	1.669	0	0.0112
B	3	3	7.069	2.403	0	0.0162
B	4	3.5	9.621	3.271	0	0.0220
B	5	3.5	9.621	3.271	0	0.0220
B	6	4	12.566	4.272	0	0
C	1	2	3.142	1.068	0.0261	0.0072
C	2	2.5	4.909	1.669	0.0408	0.0225
C	3	3	7.069	2.403	0.0587	0.0324
C	4	3.5	9.621	3.271	0.0799	0.0441
C	5	3.5	9.621	3.271	0.0799	0.0441
C	6	4	12.566	4.272	0.1044	0.0576
D	1	2	3.142	1.068	0	0
D	2	2.5	4.909	1.669	0.0204	0.0225
D	3	3	7.069	2.403	0.0294	0.0324
D	4	3.5	9.621	3.271	0.0400	0.0441
D	5	3.5	9.621	3.271	0	0.0441
D	6	4	12.566	4.272	0	0.0576
E	1	2	3.142	1.068	0.0131	0.0072
E	2	2.5	4.909	1.669	0.0204	0.0112
E	3	3	7.069	2.403	0.0294	0.0324
E	4	3.5	9.621	3.271	0.0400	0.0441
E	5	3.5	9.621	3.271	0	0.0441
E	6	4	12.566	4.272	0	0.0288
F	1	2	3.142	1.068	0	0
F	2	2.5	4.909	1.669	0	0
F	3	3	7.069	2.403	0	0
F	4	3.5	9.621	3.271	0	0
F	5	3.5	9.621	3.271	0	0
F	6	4	12.566	4.272	0	0
center	1	2	3.142	1.068	0.1044	0.0863
center	2	2	3.142	1.068	0.1044	0.0863
center	3	2	3.142	1.068	0.1044	0.0863
center	4	2	3.142	1.068	0.1044	0.0863
Total			294.132	100	1	1

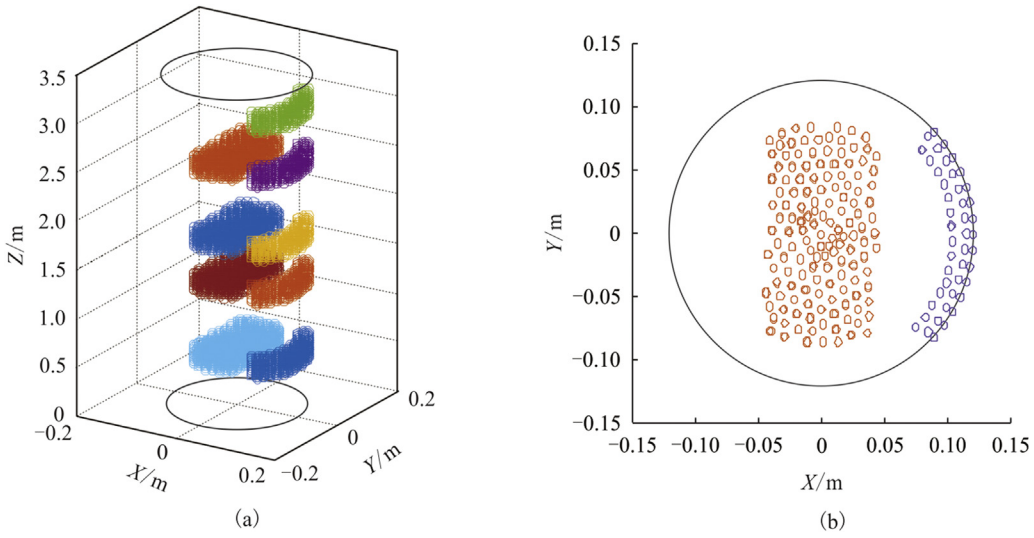

Fig. 7. Averaging mesh zones.

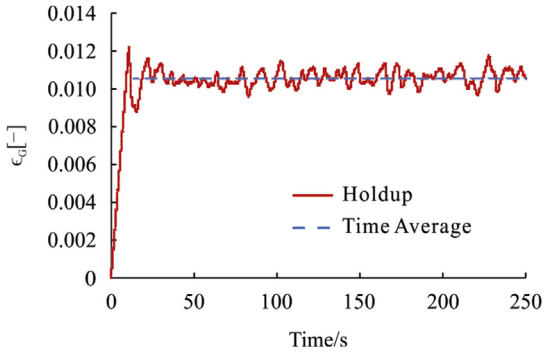

Fig. 8. Global gas holdup trend in time and time-averaged value for UG = 0.0037 m/s and standard Tomyiama lift model.

Table 6
Gas holdup: comparison between experimental results and numerical data.

U_G	Gas holdup [−]		Lift model
[m/s]	Exp	CFD	
0.0037	0.00990	0.01053	Tomiyama
		0.01054	NewLift
0.0074	0.02344	0.02097	Tomiyama
		0.02082	NewLift

the experimental and the numerical results, it is clear that the numerical result overestimates, at the wall, the contribution of the bubbles belonging to the fifth size group, corresponding to a mean diameter of 5 mm. The overestimation of the fifth bubble size group results in an over predicted peak in the BSDs: probably, this is the result of a region where breakup has just occurred and the resulting small bubbles still have to migrate towards the wall section. In addition, the numerical model is unable to predict the larger bubbles, present in the largest size groups, whereas the experimental observations indicated the presence of such larger bubbles, especially at the center region. These large and deformed bubbles are important because of their large volume, thus, they significantly affect the flow field of both phases. Nevertheless, the population balance model used for the calculations considers such structures as large and unstable bubbles, which have been consequently destroyed due to breakup. Another important remark is that both the numerical BSD and size fraction profiles significantly change, mainly, in the first and second position from the bottom; above this region, they tend to stabilize. Indeed, the CFD model does not account for disequilibrium due to the sudden coalescence and the formation of unstable gas structures: once the prevailing bubble size distribution reaches the equilibrium, it does not changes anymore. Despite the detailed inlet boundary condition for the gas phase the numerical BSDs after 35 cm are already is off. This results confirm one of the conclusions proposed in our previous numerical paper: inlet boundary conditions in large-scale bubble column seems to have secondary influence on the numerical results. However, despite the inlet BSDs have minor influence on the results, a precise modeling of inlet BSDs would provide better numerical results. Therefore, Eq. (1) and Table 1 are suggested to be used for the modeling of "*industrial-scale*" bubble columns in future studies. In conclusion, both the flow rate simulated led to acceptable results, that approximate experimental data fairly well, considered the complexity of the problem and the simplicity of the Euler-Euler approach that was used.

5.3. Local void fraction

5.3.1. Comparison between numerical and experimental results

Fig. 13 compares the experimental [2] and the numerical void fraction profiles. It is worth noting, when analyzing this comparison it should be noted that these data belongs to two different experimental campaigns: therefore, results are likely to show some differences. Generally, the numerical prediction slightly improved compared with our previous numerical paper [3], owing to the improved inlet conditions. The numerical profiles in Fig. 13a are clearly influenced by the gas sparger region; conversely, in the developed region, the void fraction profiles are almost symmetrical in shape. The discrepancies between the experimental and the numerical results in Fig. 13a are, possibly, related to the fact that results come from two different experimental campaigns. It is

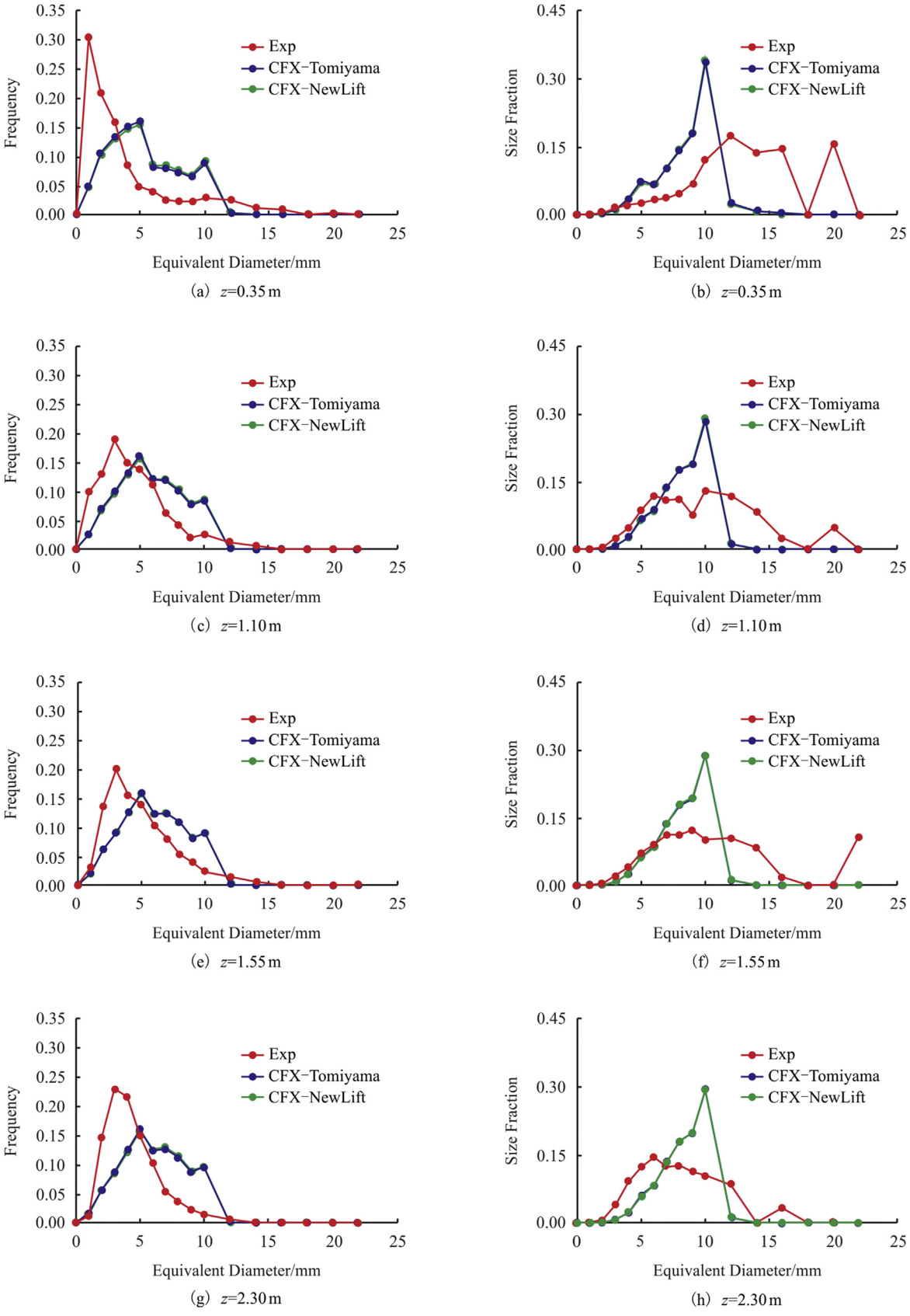

Fig. 9. Simulation results in terms of size fractions and diameter BSD at the center section, different heights and $U_G = 0.0037$ m/s.

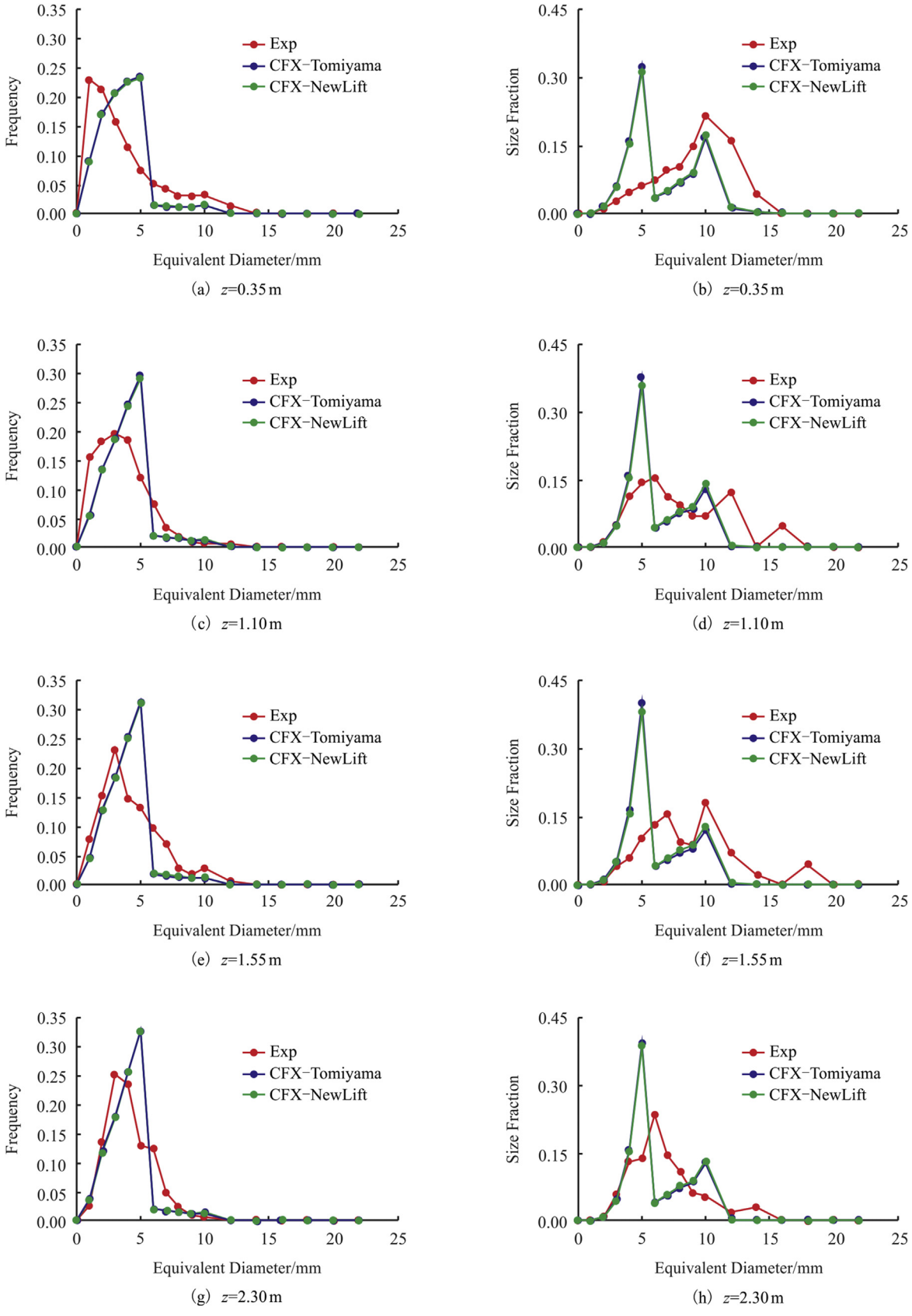

Fig. 10. Simulation results in terms of size fractions and diameter BSD at the wall section, different heights and UG = 0.0037 m/s.

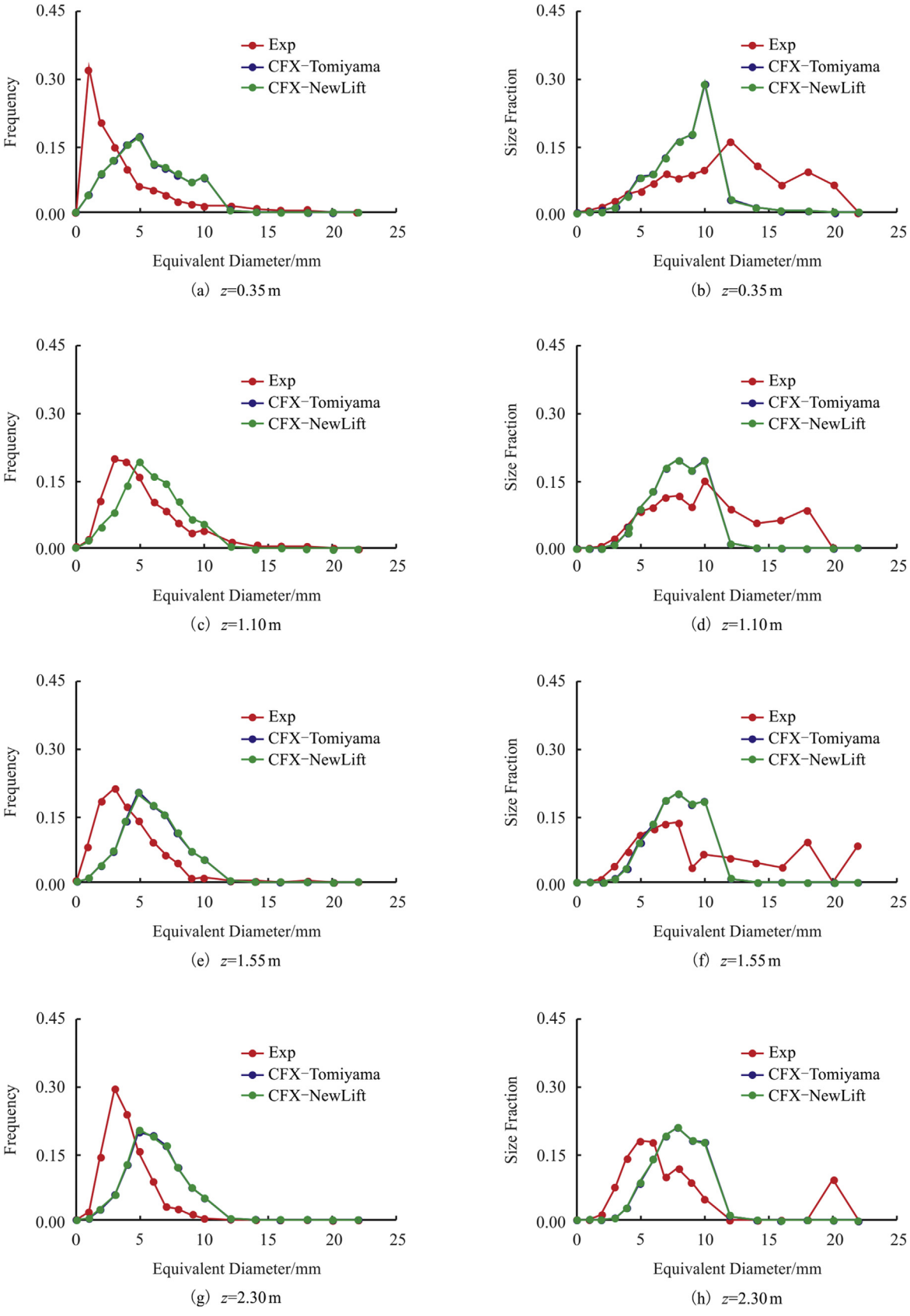

Fig. 11. Simulation results in terms of size fractions and diameter BSD at the center section, different heights and UG = 0.0074 m/s.

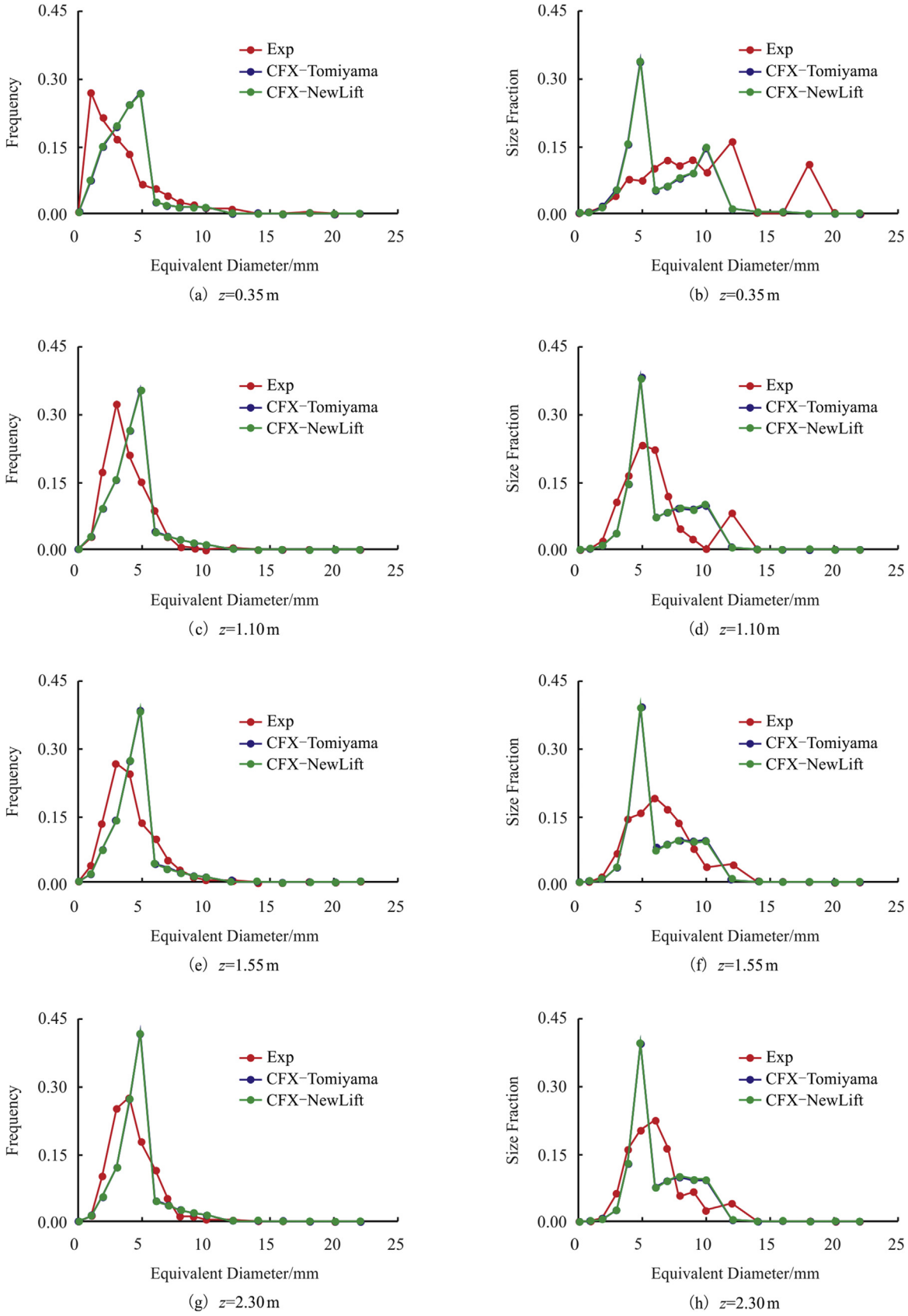

Fig. 12. Simulation results in terms of size fractions and diameter BSD at the wall section, different heights and UG = 0.0074 m/s.

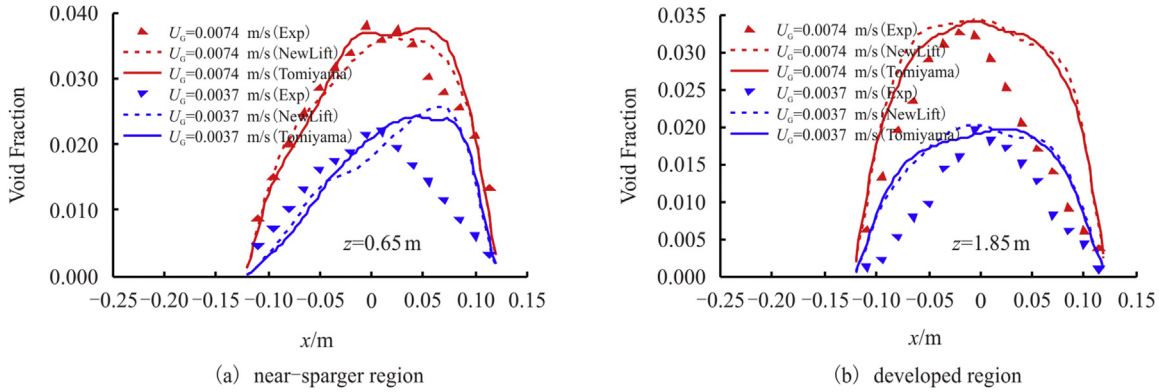

Fig. 13. Comparison between optical probe data and numerical results.

interesting to observed that the numerical approach, after reaching the coalescence-breakup equilibrium in the developed flow, is not more influenced by the gas maldistribution in the input region (Section 5.2). Conversely, the experimental data are still, even if slightly, influenced by the gas maldistribution at a considerably distance from the gas sparger. The numerical results show parabolic profile, which is consistent with the ideal behavior of the system; conversely, the experimental data are triangular shaped, as if very large fast-rising bubbles were present at the center, this increasing the local holdup. Triangular-shape void fraction profiles were also discussed in the pioneering study of Zuber and Findlay [48]. Therefore, we may state that a limitation of the CFD approach is the prediction of the very large bubbles: bubbles larger than a certain threshold value are always destroyed since unstable while, in reality, their lifetime is much wider and they can raise the column in the center section. Finally, the NewLift model does not yield appreciable improvements over the classical one. Indeed, both size fraction and BSD profiles resulting from the two simulations are almost identical. It can only be noticed, in the new lift profiles, a slight decrease of the size fraction and BSD of the last size groups of the first velocity group (4 and 5) and a likewise increase for the first of the second one (from 6 to 10). This is explained by the fact that the sign inversion of the lift coefficient happens at a slightly smaller diameter with respect to the classical Tomiyama et al. model. Therefore, a smaller fraction of bubbles (or gas volume) migrates towards the wall, leaving more possibility for coalescence in the center and the formation of bigger bubbles. In this sense, the new lift model leads to size fraction profiles that slightly better approximate the experimental ones.

5.3.2. *Axial evolution of the local void fraction profiles*

Fig. 14 displays the axial evolution of the local void fractions. As shown in Fig. 14, the way the flow rate enters the column through the gas sparger is strongly asymmetric according to the evidences acquired during the experimental campaign by visual observation. This is reflected in the simulations for both the single velocity groups and both the two groups. It is observed that the development length of the two phase flow: after approximately 1.5 m from the sparger the memory of the inlet distribution provided at the sparger is lost and the void fraction profiles become symmetric and constant in the higher region of the column. This observation is in agreement with the findings of the image analysis, where a development region of about 1 m was experimentally observed. In Fig. 14 the behavior of small bubbles is observed: according to Tomiyama et al. (2002), small bubbles are subject to the positive lift force and migrate towards the wall. In addition, at the wall bubbles have to face the wall lubrication force, which prevents them from actually touching the wall due to surface tension forces. The result is a small bubbles void fraction in the center and very close to the walls, while a peak is formed in the near wall region. This is in

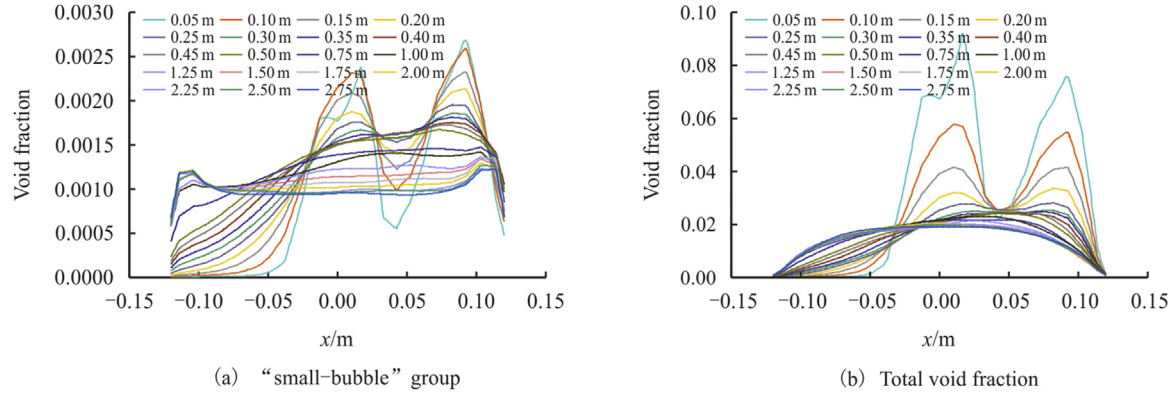

Fig. 14. Axial evolution of the void fraction.

accordance, for example, with the findings of [20].

6. Conclusions

This study concerns the prediction of the bubble size distributions in the "*pseudo-homogeneous*" flow regime, which is characterized by a wide spectrum of bubble sizes and is generally observed in industrial applications. In particular, this study aims to extent the validation of a previously proposed approach to propose a further step towards the simulation of large-scale bubble column reactors and provide clear guidelines to simulate industrial scale reactors, within the boundaries of the "*pseudo-homogeneous*" flow regime.

The main results are as follows:

(1) The comprehensive bubble size distribution dataset obtained may serve as basis to improve the coalescence and break-up closures;
(2) The precise characterization of the gas sparger served as an improved input to the numerical simulations (Eq. (1) along with Table 1);
(3) In the poly-dispersed formulation with bubble coalescence and break-up closures, the BSD used as input has secondary effect on the numerical results, compared with other closures. However, a precise implementation of the BSD at bubble column inlet is of fundamental importance for an accurate model of the bubble column fluid dynamics;
(4) The validation of a previously proposed approach has been extended to by comparing experimental and numerical bubble size distributions at different axial positions in a large-diameter and large-scale bubble column
(5) The numerical results approximate the experimental data fairly well, considered the complexity of the problem and the simplicity of the Euler-Euler approach that was used
(6) A modified lift force law has been proposed and implemented, but it does not provide considerable advancements compared with the well known Tomiyama et al. (2002) lift force.

References

[1] Y.T. Shah, B.G. Kelkar, S.P. Godbole, W.D. Deckwer, Design parameters estimations for bubble column reactors, AIChE J. 28 (3) (1982) 353–379.
[2] G. Besagni, F. Inzoli, Comprehensive experimental investigation of counter-current bubble column hydrodynamics: holdup, flow regime transition, bubble size distributions and local flow properties, Chem. Eng. Sci. 146 (2016) 259–290.
[3] G. Besagni, F. Inzoli, T. Ziegenhein, D. Lucas, Computational Fluid-Dynamic modeling of the pseudo-homogeneous flow regime in large-scale bubble columns, Chem. Eng. Sci. 160 (2017) 144–160.
[4] P.M. Wilkinson, A.P. Spek, L.L. van Dierendonck, Design parameters estimation for scale-up of high-pressure bubble columns, AIChE J. 38 (1992) 544–554.
[5] G. Besagni, F. Inzoli, The effect of liquid phase properties on bubble column fluid dynamics: gas holdup, flow regime transition, bubble size distributions and shapes, interfacial areas and foaming phenomena, Chem. Eng. Sci. 170 (2017) 270–296.
[6] G. Besagni, F. Inzoli, The effect of electrolyte concentration on counter-current gas-liquid bubble column fluid dynamics: gas holdup, flow regime transition and bubble size distributions, Chem. Eng. Res. Des. 118 (2017) 170–193.
[7] G. Besagni, F. Inzoli, G. De Guido, L.A. Pellegrini, The dual effect of viscosity on bubble column hydrodynamics, Chem. Eng. Sci. 158 (2017) 509–538.
[8] K. Akita, F. Yoshida, Gas holdup and volumetric mass transfer coefficient in bubble columns. Effects of liquid properties, Ind. Eng. Chem. Process Des. Dev. 12 (1) (1973) 76–80.
[9] T. Otake, S. Tone, K. Nakao, Y. Mitsuhashi, Coalescence and breakup of bubbles in liquids, Chem. Eng. Sci. 32 (4) (1977) 377–383.
[10] C. Cao, L. Zhao, D. Xu, Q. Geng, Q. Guo, Investigation into bubble size distribution and transient evolution in the sparger region of Gas– liquid external loop airlift reactors, Ind. Eng. Chem. Res. 48 (12) (2009) 5824–5832.
[11] T. Tate, On the magnitude of a drop of liquid formed under different circumstances, Lond., Edinb., and Dublin Philos. Mag. J. Sci. 27 (181) (1864) 176–180.
[12] G. Besagni, A. Di Pasquali, L. Gallazzini, E. Gottardi, L.P.M. Colombo, F. Inzoli, The effect of aspect ratio in counter-current gas-liquid bubble columns: experimental results and gas holdup correlations, Int. J. Multiphas. Flow 94 (2017) 53–78.
[13] M. Ishii, T. Hibiki, Thermo-fluid Dynamics of Two-phase Flow, Springer-Verlag New York, 2011.
[14] T. Ziegenhein, Fluid Dynamics of Bubbly Flows, Technische Universität Berlin, 2016.
[15] T. Ziegenhein, R. Rzehak, D. Lucas, Transient simulation for large scale flow in bubble columns, Chem. Eng. Sci. 122 (2015) 1–13.
[16] T. Ziegenhein, D. Lucas, R. Rzehak, E. Krepper, Closure relations for CFD simulation of bubble columns, in: 8th International Conference on Multiphase Flow. ICMF 2013, 2013. Jeju (Korea).
[17] R. Rzehak, S. Kriebitzsch, Multiphase CFD-simulation of bubbly pipe flow: a code comparison, Int. J. Multiphas. Flow 68 (2015) 135–152.
[18] R. Rzehak, E. Krepper, C. Lifante, Comparative study of wall-force models for the simulation of bubbly flows, Nucl. Eng. Des. 253 (2012) 41–49.
[19] R. Rzehak, E. Krepper, Y. Liao, T. Ziegenhein, S. Kriebitzsch, D. Lucas, Baseline model for the simulation of bubbly flows, Chem. Eng. Technol. 38 (11) (2015) 1972–1978.
[20] R. Rzehak, E. Krepper, Closure models for turbulent bubbly flows: a CFD study, Nucl. Eng. Des. 265 (2013) 701–711.
[21] D. Lucas, R. Rzehak, E. Krepper, T. Ziegenhein, Y. Liao, S. Kriebitzsch, P. Apanasevich, A strategy for the qualification of multi-fluid approacheds for nuclear reactor safety, Nucl. Eng. Des. 299 (2016) 2–11.
[22] Y. Liao, R. Rzehak, D. Lucas, E. Krepper, Baseline closure model for dispersed bubbly flow: bubble coalescence and breakup, Chem. Eng. Sci. 122 (2015) 336–349.
[23] J. Liao, T. Ziegenhein, R. Rzehak, Bubbly flow in an airlift column: a CFD study, J. Chem. Technol. Biotechnol. 91 (2016) 2904–2915.
[24] R. Rzehak, E. Krepper, CFD modeling of bubble-induced turbulence, Int. J. Multiphas. Flow 55 (2013) 138–155.
[25] M. Pourtousi, J.N. Sahu, P. Ganesan, Effect of interfacial forces and turbulence models on predicting flow pattern inside the bubble column, Chem. Eng. Process: Process Intensif. 75 (0) (2014) 38–47.
[26] M. Ishii, N. Zuber, Drag coefficient and relative velocity in bubbly, droplet or particulate flows, AIChE J. 25 (5) (1979) 843–855.
[27] D. Lucas, H.M. Prasser, A. Manera, Influence of the lift force on the stability of a bubble column, Chem. Eng. Sci. 60 (13) (2005) 3609–3619.
[28] A. Tomiyama, H. Tamai, I. Zun, S. Hosokawa, Transverse migration of single bubbles in simple shear flows, Chem. Eng. Sci. 57 (11) (2002) 1849–1858.
[29] J. Lu, S. Biswas, G. Tryggvason, A DNS study of laminar bubbly flows in a vertical channel, Int. J. Multiphas. Flow 32 (6) (2006) 643–660.
[30] J. Lu, G. Tryggvason, Effect of bubble size in turbulent bubbly downflow in a vertical channel, Chem. Eng. Sci. 62 (11) (2007) 3008–3018.
[31] J. Lu, G. Tryggvason, Dynamics of nearly spherical bubbles in a turbulent channel upflow, J. Fluid Mech. 732 (2013) 166–189.
[32] C. Santarelli, J. Fröhlich, Direct Numerical Simulations of spherical bubbles in vertical turbulent channel flow. Influence of bubble size and bidispersity, Int. J. Multiphas. Flow 81 (2016) 27–45.
[33] R.M. Wellek, A.K. Agrawal, A.H.P. Skelland, Shape of liquid drops moving in liquid media, AIChE J. 12 (5) (1966) 854–862.
[34] G. Besagni, F. Inzoli, Bubble size distributions and shapes in annular gap bubble column, Exp. Therm. Fluid Sci. 74 (2016) 27–48.
[35] D. Lucas, A. Tomiyama, On the role of the lateral lift force in poly-dispersed bubbly flows, Int. J. Multiphas. Flow 37 (9) (2011) 1178–1190.
[36] S. Hosokawa, A. Tomiyama, S. Misaki, T. Hamada, Lateral migration of single bubbles due to the presence of wall, in: ASME 2002 Joint US-european Fluids Engineering Division Conference, American Society of Mechanical Engineers, 2002, pp. 855–860.
[37] A. Tomiyama, A. Sou, I. Zun, N. Kanami, T. Sakaguchi, Effects of Eötvös number and dimensionless liquid volumetric flux on lateral motion of a bubble in a laminar duct flow, in: A.S.F. Bataille (Ed.), Multiphase Flow 1995, Elsevier, Amsterdam, 1995, pp. 3–15.
[38] A.D. Burns, T. Frank, I. Hamill, J.-M. Shi, The Favre averaged drag model for turbulent dispersion in Eulerian multi-phase flows, in: 5th International Conference on Multiphase Flow, ICMF'04 Yokohama (Japan), 2004.
[39] G. Mougin, J. Magnaudet, The generalized Kirchhoff equations and their application to the interaction between a rigid body and an arbitrary time-dependent viscous flow, Int. J. Multiphas. Flow 28 (11) (2002) 1837–1851.
[40] E. Krepper, D. Lucas, T. Frank, H.-M. Prasser, P.J. Zwart, The inhomogeneous MUSIG model for the simulation of polydispersed flows, Nucl. Eng. Des. 238 (7) (2008) 1690–1702.
[41] Y. Liao, D. Lucas, A literature review on mechanisms and models for the coalescence process of fluid particles, Chem. Eng. Sci. 65 (10) (2010) 2851–2864.
[42] Y. Liao, D. Lucas, A literature review of theoretical models for drop and bubble breakup in turbulent dispersions, Chem. Eng. Sci. 64 (15) (2009) 3389–3406.
[43] D. Pfleger, S. Gomes, N. Gilbert, H.G. Wagner, Hydrodynamic simulations of

laboratory scale bubble columns fundamental studies of the Eulerian–Eulerian modelling approach, Chem. Eng. Sci. 54 (21) (1999) 5091–5099.
[44] A. Sokolichin, G. Eigenberger, Applicability of the standard k–ε turbulence model to the dynamic simulation of bubble columns: Part I. Detailed numerical simulations, Chem. Eng. Sci. 54 (13–14) (1999) 2273–2284.
[45] R.F. Mudde, O. Simonin, Two- and three-dimensional simulations of a bubble plume using a two-fluid model, Chem. Eng. Sci. 54 (21) (1999) 5061–5069.
[46] K. Ekambara, M.T. Dhotre, J.B. Joshi, CFD simulations of bubble column reactors: 1D, 2D and 3D approach, Chem. Eng. Sci. 60 (23) (2005) 6733–6746.
[47] Y. Waghmare, C. Dorao, H. Jakobsen, F.C. Knopf, R. Rice, Bubble size distribution for a bubble column reactor undergoing forced oscillations, Ind. Eng. Chem. Res. 48 (4) (2009) 1786–1796.
[48] N. Zuber, J.A. Findlay, Average volumetric concentration in two-phase flow systems, J. Heat Tran. 87 (4) (1965) 453–468.